

# A Heavy Ion Fireball freeze-out Dipion Cocktail for Au-Au Collisions at $\sqrt{s_{NN}}=200$ GeV $p_t$ dependence(Part 2).

R.S. Longacre<sup>a</sup>

<sup>a</sup>Brookhaven National Laboratory, Upton, NY 11973, USA

## Abstract

In this paper we use methods developed in Part 1 of The Dipion Cocktail, to fit the  $p_t$  dependence of dipions for mid-central Au-Au collisions at  $\sqrt{s_{NN}}=200$  GeV. For the minijet fragmentation part we use PYTHIA fragmentation as described in Part 1. For the thermal resonance production we use an exponential growth behavior. The interference between the direct production of dipion pairs from non-resonance minijet fragmentation and re-scattering through resonance states gives a measure of the size of the re-scattering region. This size is contained in the  $\alpha$  parameter of Part1. We assumed a relationship between the  $\alpha$  parameter and the mass shift of the  $\rho$  resonance. The data used for the fits comes from the RHIC collider as measured in the STAR experiment.

## 1 Introduction

The ultra-relativistic heavy ion collision starts out as a state of high density nuclear matter called the Quark Gluon Plasma(QGP) and expands rapidly to freeze-out. During the freeze-out phase quarks and gluons form a system of strongly interacting hadrons. These hadrons continue to expand in a thermal manner until no further scattering is possible because the system becomes too dilute. However this transition from quarks and gluons(partons) into hadrons is not a smooth affair. The expansion is very rapid and some faster or hard scattered partons fragment directly into hadron through a minijet[1] process. Thus we have thermal and minijet hadrons present in the last scattering of the hadrons. The Dipion Cocktail Part 1 considered this mixture of sources and applied it to the dipion mass spectrum of the heavy ion fireball formed in Au-Au collisions at  $\sqrt{s_{NN}}=200$ . Part 1 showed that both thermal or soft production of hadrons and the minijet fragmented hadrons can be described through a set of unified formal equations. Part 2(this paper) applies this formalism to the  $p_t$  dependence of dipions for Au-Au collisions at  $\sqrt{s_{NN}} = 200$  GeV and 40% to 80% centrality.

The paper is organized in the following manner:

Sec. 1 Introduction. Sec. 2 Review of the two component model which we use to fit the dipion data within a set of  $p_t$  ranges. Sec. 3 Discussion of the relationship between the  $\alpha$  parameter and the mass and widths of resonances. Sec. 4 we present a fit to 19  $p_t$  ranges for Au-Au collisions at  $\sqrt{s_{NN}} = 200$  GeV and 40% to 80% centrality. Sec. 5 Summary and Discussion.

## 2 Two component model with Breit-Wigner parameters

In this section we will alter equation 6 of Part 1 so it can use Breit-Wigner parameters (mass, width) instead of phase shifts. We will also need to modify the re-scattering part of the equation in order to have the correct threshold behavior we have introduced in Part 1 for the minijet partial waves. The phase shift can be written for the  $\ell^{th}$  wave as

$$\cot\delta_\ell = \frac{(M_\ell^2 - M_{\pi\pi}^2)}{M_\ell\Gamma_\ell}, \quad (1)$$

where  $M_\ell$  is the mass of the resonance in the  $\ell$  wave and  $\Gamma_\ell$  is its total width.

$$\Gamma_\ell = \Gamma_{0\ell} \frac{\frac{qB_\ell(q/q_s)}{M_{\pi\pi}}}{\frac{q_\ell B_\ell(q_\ell/q_s)}{M_\ell}} \quad (2)$$

with  $\Gamma_{0\ell}$  the total width at resonance,  $B_\ell$  is the Blatt-Weisskopf-barrier factor[2] for the  $\ell$  of the resonance,  $q$  is the  $\pi\pi$  center mass momentum,  $q_\ell$  is  $q$  at resonance,  $M_\ell$  is the mass of the resonance, and  $q_s$  is center mass momentum related to the size(1.0 fm is used  $q_s = .200$  GeV/c).

Using equation 1 we rewrite equation 6 of Part 1 as

$$|T_\ell|^2 = |D_\ell|^2 \frac{\sin^2\delta_\ell}{PS_\ell} + \frac{|A_\ell|^2 \sin^2\delta_\ell}{PS_\ell} |\alpha + PS_\ell \cot\delta_\ell|^2 \quad (3)$$

The  $D_\ell$  is the thermal production term and is constant except for the Boltzmann weight(see equation 13 in Part 1). The expected threshold behavior  $q^{2\ell+1}$  comes from the  $\sin\delta_\ell$  term. Since there is  $\sin^2\delta_\ell$  one of the  $q^{2\ell+1}$  is killed off by dividing by  $PS_\ell$ . In Figure 6 of Part 1 we see we have put into our minijet  $A_\ell$  the correct threshold  $q^{2\ell+1}$  so we need to kill off the  $q^{2\ell+1}$  of the other  $\sin\delta_\ell$  term. Therefore the above equation for our minijet  $A_\ell$  we will use

$$|T_\ell|^2 = |D_\ell|^2 \frac{\sin^2\delta_\ell}{PS_\ell} + \frac{|A_\ell|^2 \sin^2\delta_\ell}{PS_\ell^2} |\alpha + PS_\ell \cot\delta_\ell|^2 \quad (4)$$

Rewriting equation 6 of Part 1 for each partial wave with Breit-Wigner parameters the first term becomes

$$|T_{\ell 1}|^2 = |D_\ell|^2 \frac{M_{\pi\pi}^2}{\sqrt{M_{\pi\pi}^2 + p_t^2}} \exp\left(-\frac{\sqrt{M_{\pi\pi}^2 + p_t^2}}{T}\right) \frac{M_\ell\Gamma_\ell}{(M_\ell^2 - M_{\pi\pi}^2)^2 + M_\ell^2\Gamma_\ell^2}, \quad (5)$$

while the second term

$$|T_{\ell 2}|^2 = |A_\ell|^2 \frac{M_\ell^2\Gamma_\ell^2}{(M_\ell^2 - M_{\pi\pi}^2)^2 + M_\ell^2\Gamma_\ell^2} \left| \alpha + \frac{2qB_\ell(\frac{q}{q_s})(M_\ell^2 - M_{\pi\pi}^2)}{M_{\pi\pi}M_\ell\Gamma_\ell} \right|^2 \left( \frac{M_{\pi\pi}^2}{4q^2B_\ell^2(\frac{q}{q_s})} \right). \quad (6)$$

$$|T|^2 = \sum_{\ell} |T_{\ell}|^2 \quad (7)$$

where

$$|T_{\ell}|^2 = |T_{\ell}|_1^2 + |T_{\ell}|_2^2 \quad (8)$$

and  $|A_0|^2 = S(M_{\pi^+\pi^-})$ ,  $|A_1|^2 = P(M_{\pi^+\pi^-})$ ,  $|A_2|^2 = D(M_{\pi^+\pi^-})$ , and  $|A_3|^2 = F(M_{\pi^+\pi^-})$ . S, P, D and F comes from subsection 5.2 of Part 1.

### 3 A Relationship between the $\alpha$ parameter and the mass and widths of resonances.

Equation 6 of Part 1 has an important factor the coefficient  $\alpha$ . This coefficient is related to the real part of the  $\pi\pi$  re-scattering loop and is given by equation 9. When the pions re-scatter or interact at a close distance or a point the real part of the loop  $\alpha$  has its maximum value of  $\alpha_0$ . While if the pions re-scatter or interact at a distance determined by the diffractive limit the value of  $\alpha$  is zero. The  $\alpha$  which is the real part of the re-scattering factor has a simple form given by

$$\alpha = (1.0 - \frac{r^2}{r_0^2})\alpha_0 \quad (9)$$

where  $r$  is the radius of re-scattering in fm's and  $r_0$  is 1.0 fm or the limiting range of the strong interaction ranging to  $r = 0.0$  for point like interactions.

When  $\pi\pi$  pairs interact at the diffractive limit their phase shift should be the same as the phase shift of the vacuum. The same statement is true for  $\pi\pi$  interacting at a point since asymptotic freedom demands that the strong interaction should have no effect. However values of  $\alpha$  in between zero and  $\alpha_0$  represent a confined volume where strongly interacting gluons, quarks and virtual mesons may influence the phase shift of the  $\pi\pi$  system. Phase shifts under a Breit-Wigner parameters assumption depend on the mass and width of the resonance parameter. In the next section we use fits to data to determine the relationship between Breit-Wigner parameters and the value of  $\alpha$ .

### 4 STAR data dipion $p_t$ range (0.2 GeV/c < $p_t$ < 4.0 GeV/c)

We have fitted 19 dipion  $p_t$  ranges(see Table I) using equation 7 above for the STAR Au-Au collisions at  $\sqrt{s_{NN}} = 200$  GeV 40% to 80% centrality data. We included minijets up to  $\ell = 3$  and resonances  $\sigma$   $\ell = 0$ ,  $\rho(770)$   $\ell = 1$ , and  $f_2(1270)$   $\ell = 2$ . Using the arguments of Sec. 3 of Part 1, we added the  $f_0$  as a direct thermal term ( $|T_0|_1^2$ ) and only the  $\sigma$  interfered with  $\ell = 0$  minijet background. Two other thermal terms are present in the cocktail, the  $k_s^0$  and

the  $\omega_0$ . All the thermal terms have an exponential behavior with dipion  $p_t$ . The spectrum of the minijet partial waves is obtained from PYTHIA[3](see Sec. 5.2 of Part 1). We let the data determine which minijet partial wave to add. We find only Swave minijet background is important until  $p_t$  equal to 1.1 GeV/c. Above 1.5 GeV/c all four minijet partial waves are used up to Fwave. It should be noted Dwave and Fwave are small effects. We used PDG[4] for the  $f_2(1270)$  mass = 1.275 GeV and width = .185 GeV. The  $f_0$  was fitted obtaining mass =  $0.9727 \pm .0039$  GeV and width =  $0.04512 \pm 0.01128$  GeV. The  $\sigma$  mass and width used was fixed because it was ill determined. The mass used was mass = 1.011 GeV and width = 1.015 GeV. The  $\rho$  mass and width is explained below.

Finally the threshold effective mass region .280 GeV to .430 GeV is dominated by the Swave and receives contributions from minijet fragmentation,  $\pi\pi$  Swave phase shift,  $\eta$  decay, HBT adding to the like sign  $\pi\pi$  distribution that has been subtracted away from the unlike sign  $\pi\pi$  and the coulomb correction between the charged pions. The minijet fragmentation is the least known of the effects since we relied on PYTHIA, however there are large uncertainty in all the other effects. So for these fits we let the minijet fragmentation be free to fit the data and let the Breit-Wigner parameters for the  $\sigma$  determine the Swave phase shifts plus leaving out all other effects.

For the  $\alpha$  parameter in  $p_t$  bins up to 1.1 GeV/c the minijet Swave interference is the determining factor. Above 1.1 GeV/c the Pwave interference becomes most important. The values of  $\alpha$  which gives a reasonable fit are shown in Table II.

We have determined that the  $\sigma$  pole or Breit-Wigner parameters is so far away from the real axis thus it is too short lived to be influenced by hadronic interactions. The  $\rho$  phase shift being of a life time comparable to hadronic interaction taking place becomes most sensitive. We have found as a function of  $\alpha$  the best of  $\rho$  width is always 0.147 GeV with an error of  $\pm .007$  GeV. The mass however decreases as  $\alpha$  grows, reaching a minimum of 0.738 GeV at an  $\alpha$  of 0.907. This is a mass shift of 37 MeV. An  $\alpha$  of 0.504 is the smallest  $\alpha$  we find in our fits. A mass of 0.775 GeV is the best fit when the value of  $\alpha$  is at 0.504. Using equation 9 in Table II we determine the radius of  $\pi\pi$  re-scattering for each  $p_t$  bin. The value of  $\alpha_0$  used in Table II is equal to 2.0 as determined in Appendix B of Part 1. Table II shows an interesting density effect around dipion  $p_t$  of 0.6 to 1.0 GeV/c. If one consider that  $p_t$  maybe related to fireball size through the idea of hubble flow, then pions with a  $p_t$  of around 0.4 GeV/c maybe coming from a less dense region in the central part of the fireball. This could be a density wave effect.

**Table I.** The  $p_t$  ranges bins we fit.

Table I		
$p_t$ bin number	lower edge(GeV/c)	upper edge(GeV/c)
1	0.2	0.4
2	0.4	0.6
3	0.6	0.8
4	0.8	1.0
5	1.0	1.2
6	1.2	1.4
7	1.4	1.6
8	1.6	1.8
9	1.8	2.0
10	2.0	2.2
11	2.2	2.4
12	2.4	2.6
13	2.6	2.8
14	2.8	3.0
15	3.0	3.2
16	3.2	3.4
17	3.4	3.6
18	3.6	3.8
19	3.8	4.0

**Table II.** The  $\alpha$  value,  $\rho$  mass value and radius in each  $p_t$  range.

Table II			
$p_t(\text{GeV}/c)$	$\alpha$	$\rho$ mass(GeV)	radius(f)
0.3	$0.907 \pm .028$	$0.738 \pm .004$	$.739 \pm .010$
0.5	$0.806 \pm .025$	$0.748 \pm .003$	$.773 \pm .008$
0.7	$0.706 \pm .022$	$0.755 \pm .002$	$.804 \pm .007$
0.9	$0.706 \pm .022$	$0.755 \pm .002$	$.804 \pm .007$
1.1	$0.806 \pm .025$	$0.748 \pm .003$	$.773 \pm .008$
1.3	$0.806 \pm .025$	$0.748 \pm .003$	$.773 \pm .008$
1.5	$0.806 \pm .025$	$0.748 \pm .003$	$.773 \pm .008$
1.7	$0.806 \pm .025$	$0.748 \pm .003$	$.773 \pm .008$
1.9	$0.806 \pm .025$	$0.748 \pm .003$	$.773 \pm .008$
2.1	$0.605 \pm .019$	$0.759 \pm .002$	$.835 \pm .006$
2.3	$0.504 \pm .016$	$0.775 \pm .001$	$.865 \pm .004$
2.5	$0.504 \pm .016$	$0.775 \pm .001$	$.865 \pm .004$
2.7	$0.504 \pm .016$	$0.775 \pm .001$	$.865 \pm .004$
2.9	$0.504 \pm .016$	$0.775 \pm .001$	$.865 \pm .004$
3.1	$0.504 \pm .016$	$0.775 \pm .001$	$.865 \pm .004$
3.3	$0.504 \pm .016$	$0.775 \pm .001$	$.865 \pm .004$
3.5	$0.504 \pm .016$	$0.775 \pm .001$	$.865 \pm .004$
3.7	$0.504 \pm .016$	$0.775 \pm .001$	$.865 \pm .004$
3.9	$0.504 \pm .016$	$0.775 \pm .001$	$.865 \pm .004$

The 19 dipion spectrum for the  $p_t$  bins are shown in Figure 1 through Figure 19.

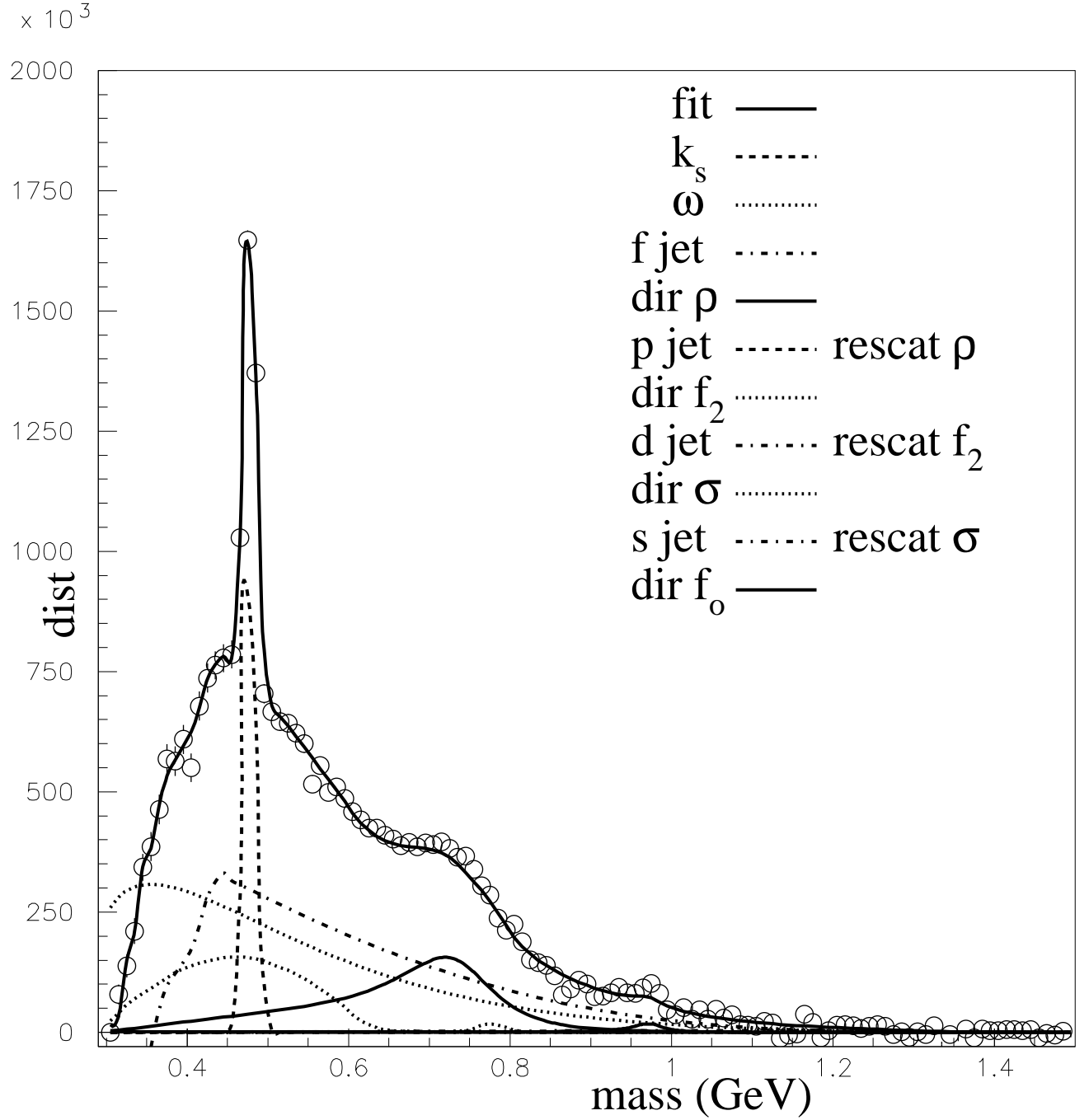


Figure 1: Fit to STAR dipion effective mass distribution ( $0.2 \text{ GeV}/c < p_t < 0.4 \text{ GeV}/c$ ) for Au-Au collisions at  $\sqrt{s_{NN}} = 200 \text{ GeV}$  40% to 80% centrality using equation 7. See text for complete information.

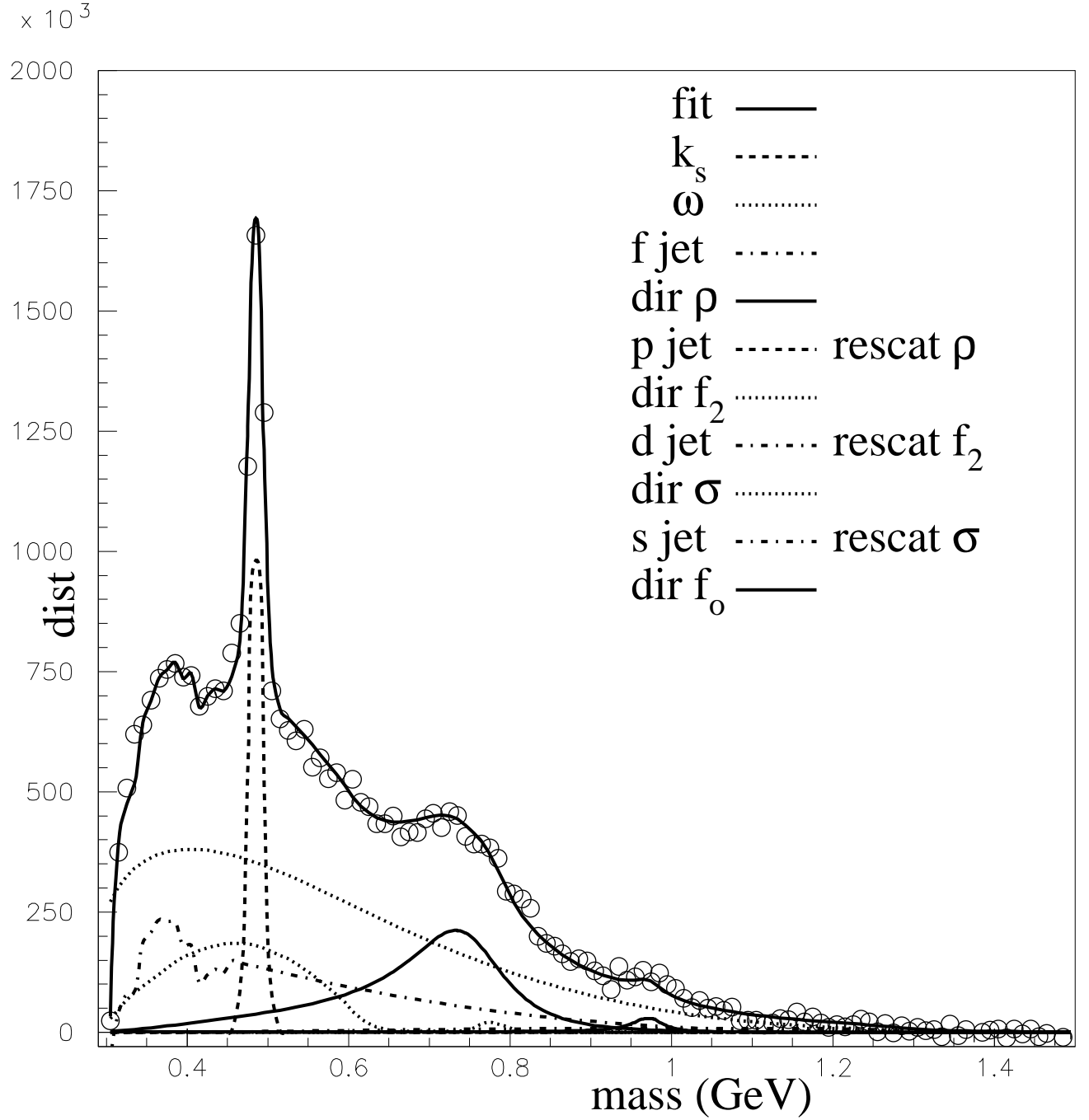


Figure 2: Fit to STAR dipion effective mass distribution ( $0.4 \text{ GeV}/c < p_t < 0.6 \text{ GeV}/c$ ) for Au-Au collisions at  $\sqrt{s_{NN}} = 200 \text{ GeV}$  40% to 80% centrality using equation 7. See text for complete information.



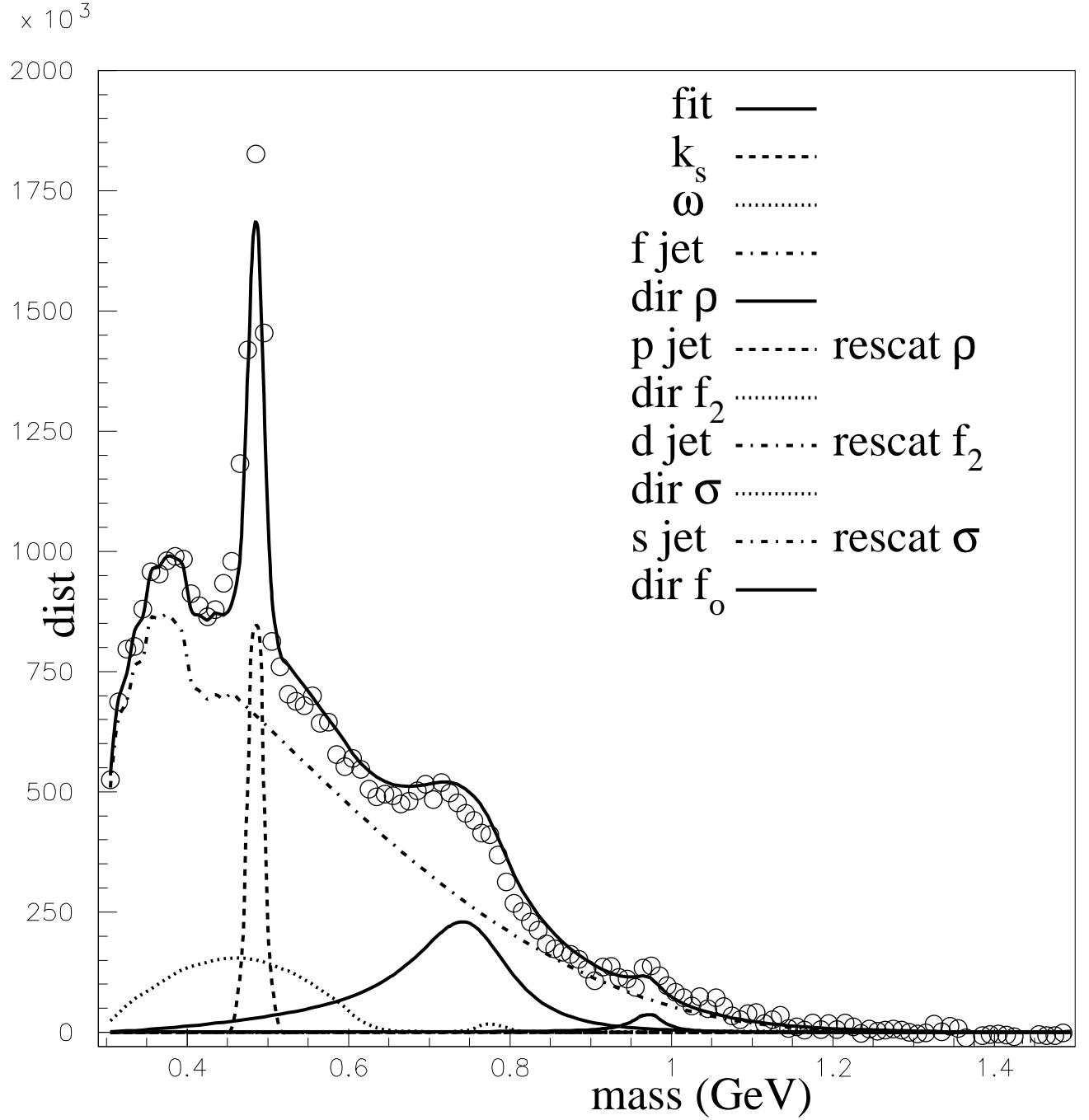


Figure 3: Fit to STAR dipion effective mass distribution ( $0.6 \text{ GeV}/c < p_t < 0.8 \text{ GeV}/c$ ) for Au-Au collisions at  $\sqrt{s_{NN}} = 200$  GeV 40% to 80% centrality using equation 7. See text for complete information.

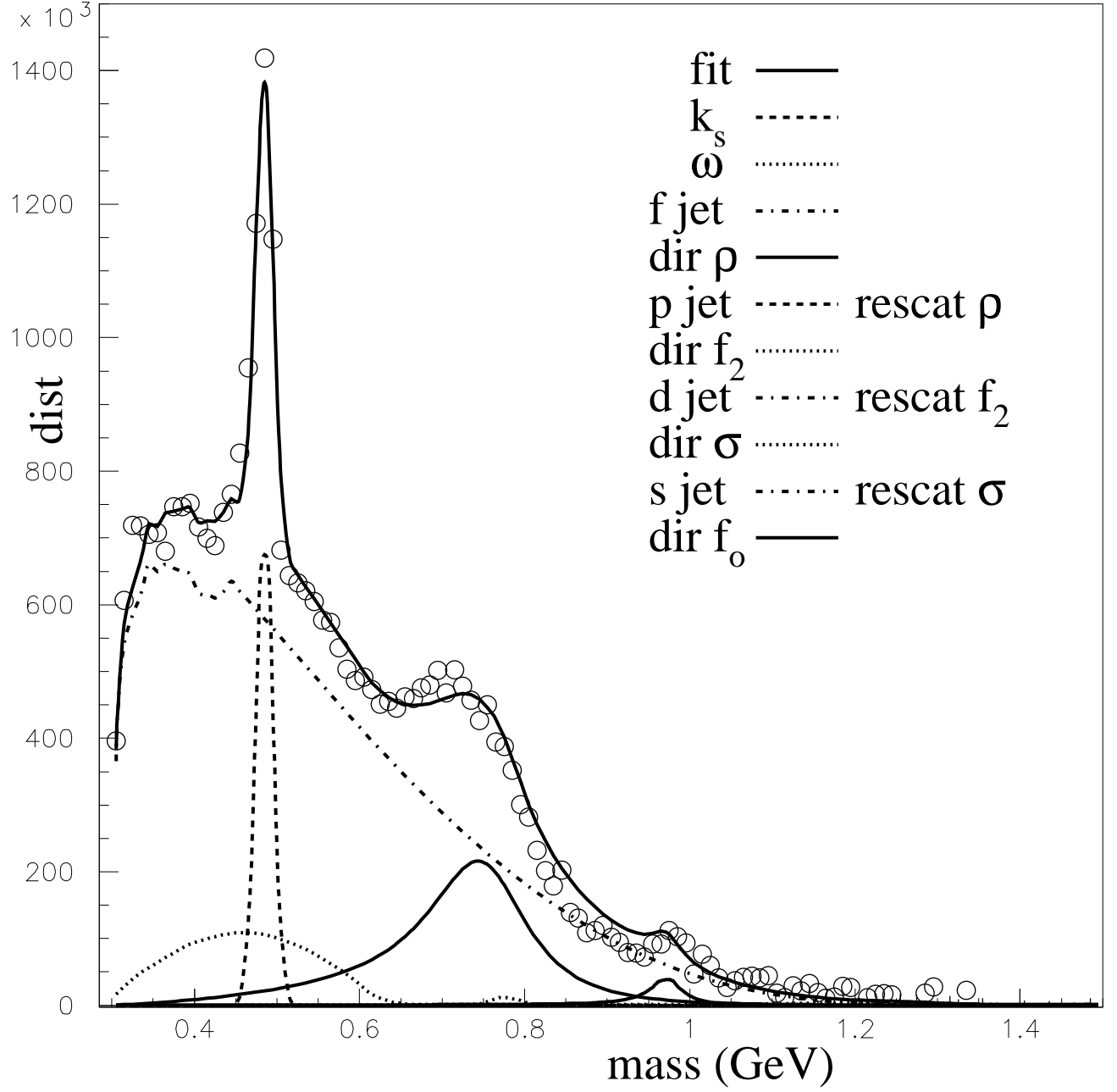


Figure 4: Fit to STAR dipion effective mass distribution ( $0.8 \text{ GeV}/c < p_t < 1.0 \text{ GeV}/c$ ) for Au-Au collisions at  $\sqrt{s_{NN}} = 200 \text{ GeV}$  40% to 80% centrality using equation 7. See text for complete information.

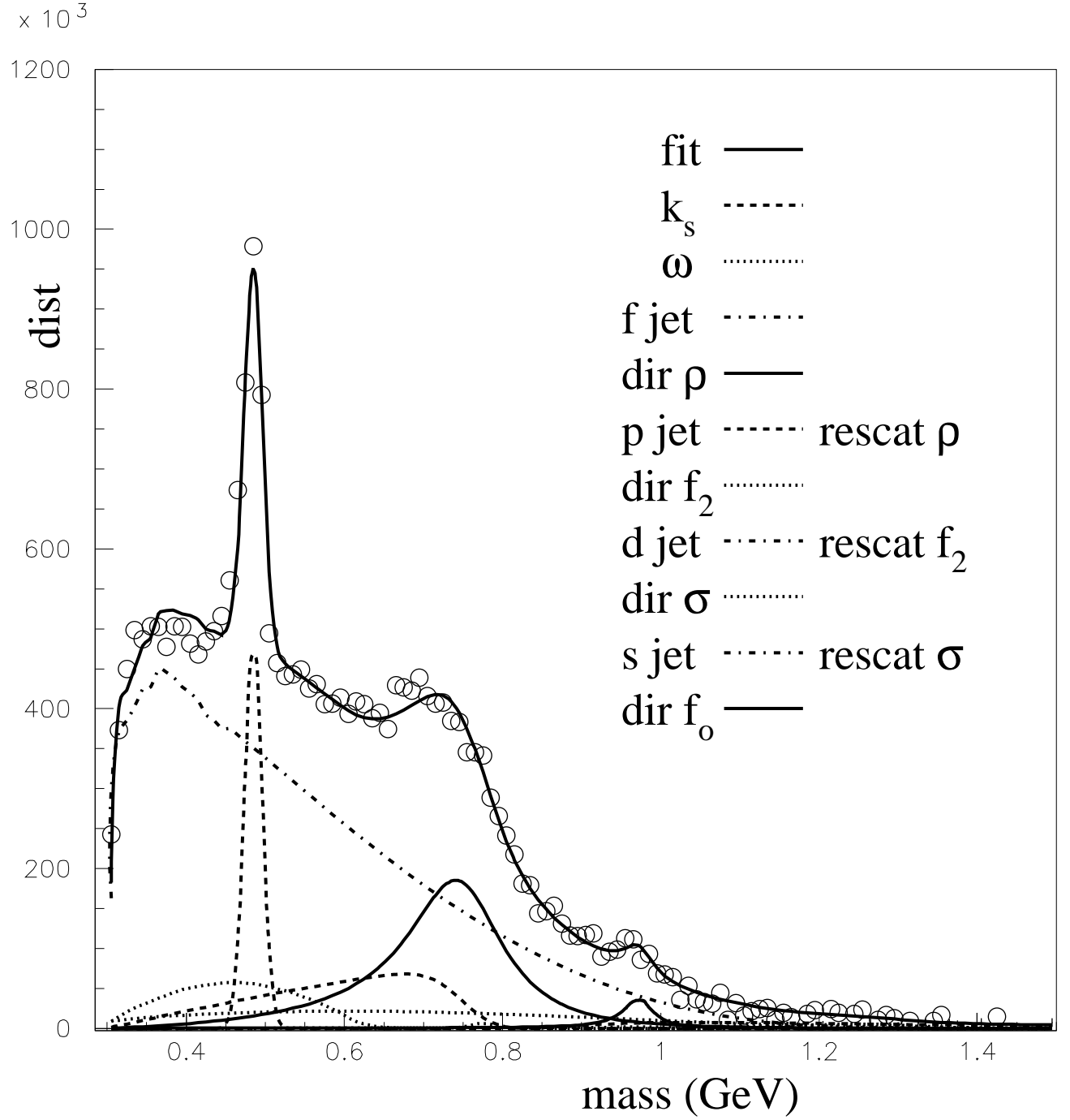


Figure 5: Fit to STAR dipion effective mass distribution ( $1.0 \text{ GeV}/c < p_t < 1.2 \text{ GeV}/c$ ) for Au-Au collisions at  $\sqrt{s_{NN}} = 200 \text{ GeV}$  40% to 80% centrality using equation 7. See text for complete information.

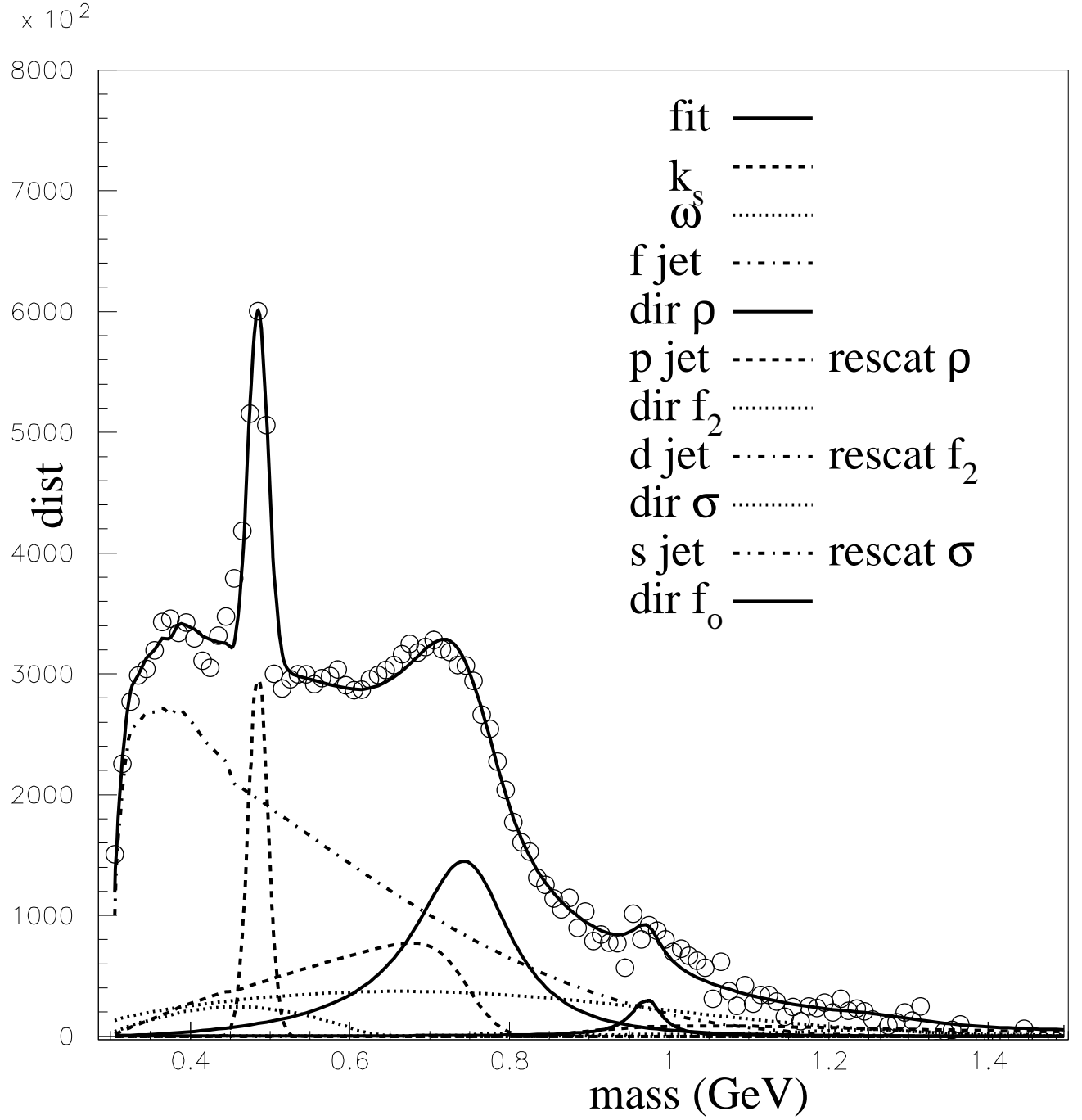


Figure 6: Fit to STAR dipion effective mass distribution ( $1.2 \text{ GeV}/c < p_t < 1.4 \text{ GeV}/c$ ) for Au-Au collisions at  $\sqrt{s_{NN}} = 200 \text{ GeV}$  40% to 80% centrality using equation 7. See text for complete information.

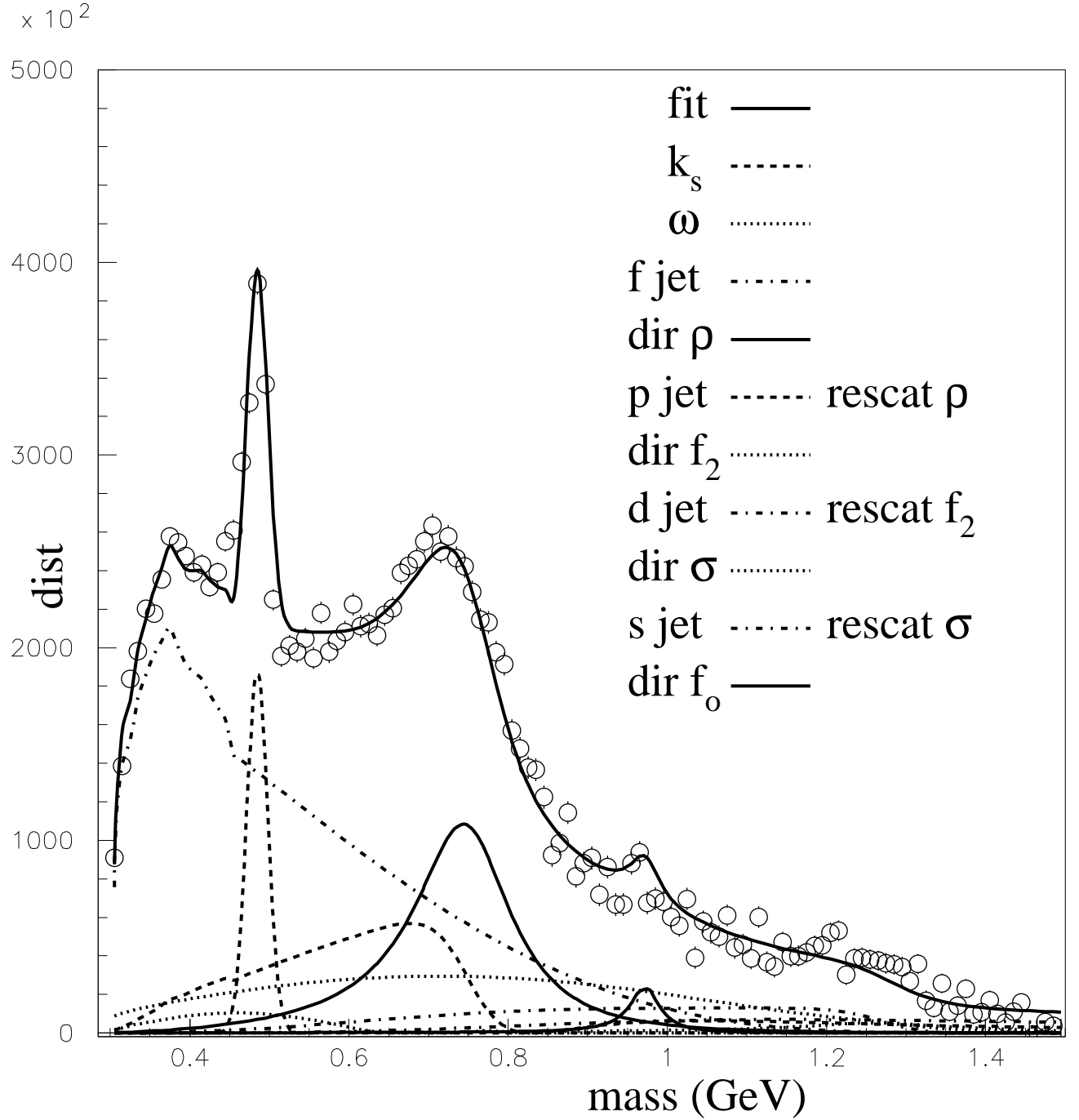


Figure 7: Fit to STAR dipion effective mass distribution ( $1.4 \text{ GeV}/c < p_t < 1.6 \text{ GeV}/c$ ) for Au-Au collisions at  $\sqrt{s_{NN}} = 200 \text{ GeV}$  40% to 80% centrality using equation 7. See text for complete information.

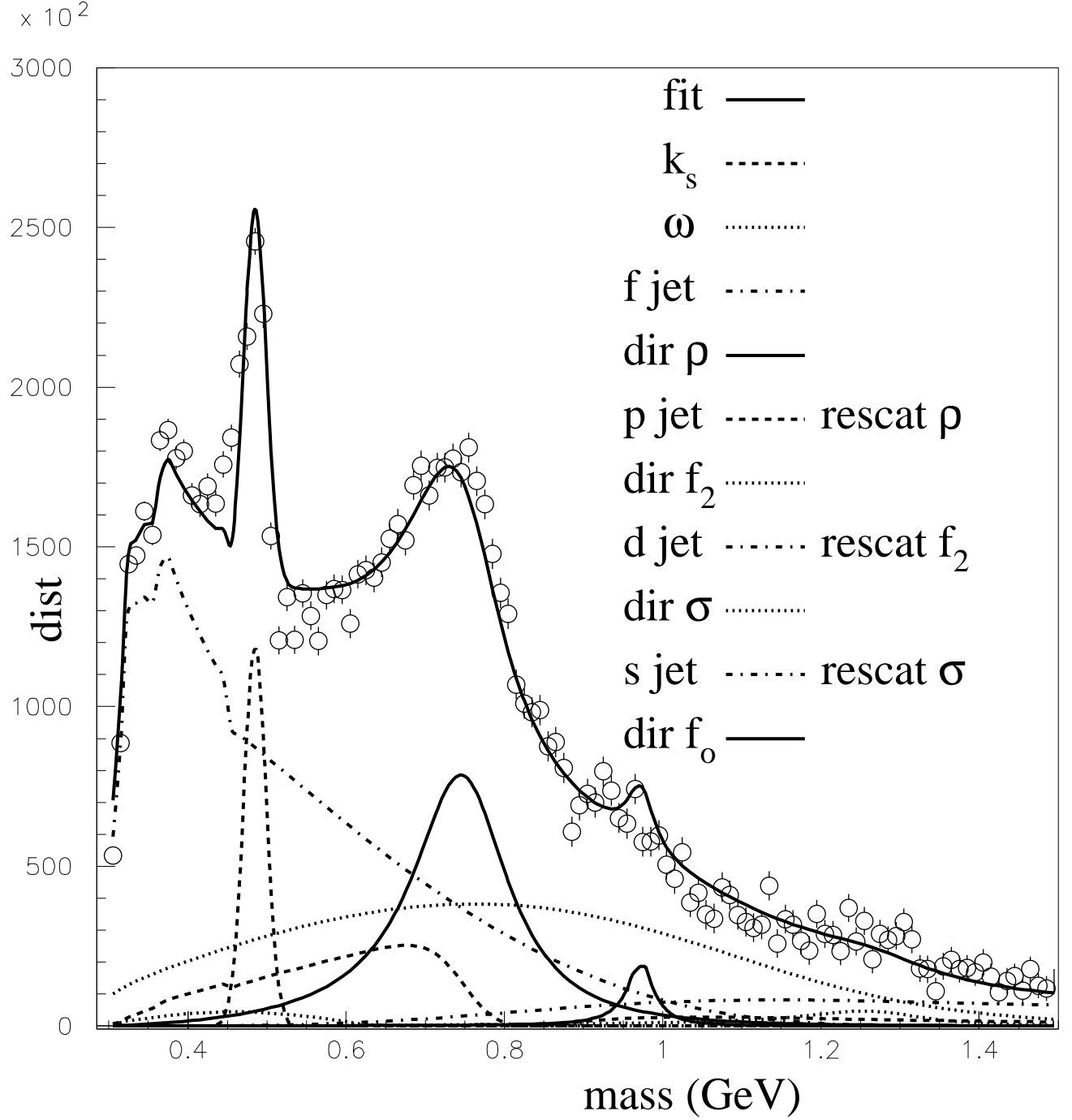


Figure 8: Fit to STAR dipion effective mass distribution ( $1.6 \text{ GeV}/c < p_t < 1.8 \text{ GeV}/c$ ) for Au-Au collisions at  $\sqrt{s_{NN}} = 200 \text{ GeV}$  40% to 80% centrality using equation 7. See text for complete information.

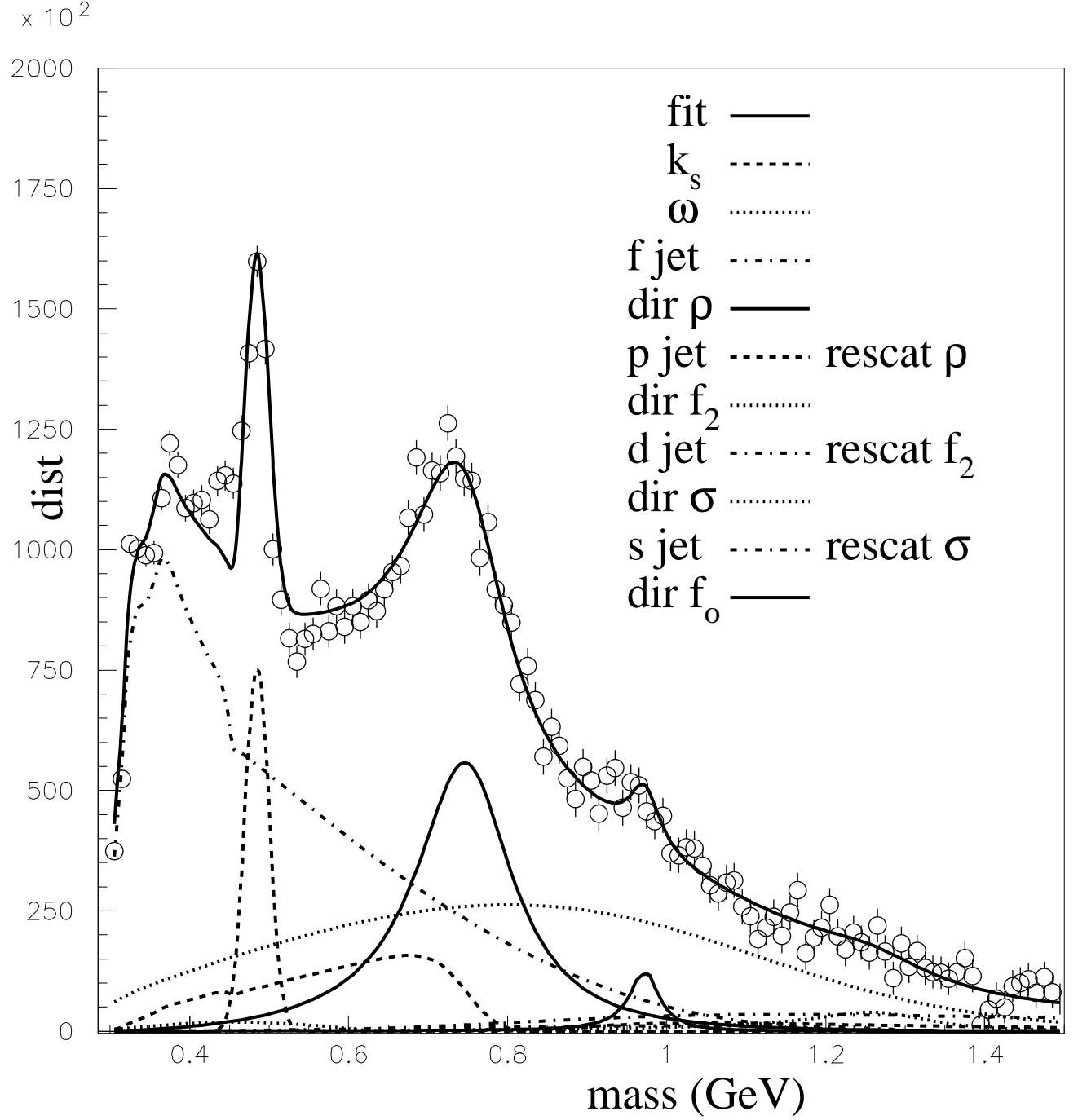


Figure 9: Fit to STAR dipion effective mass distribution ( $1.8 \text{ GeV}/c < p_t < 2.0 \text{ GeV}/c$ ) for Au-Au collisions at  $\sqrt{s_{NN}} = 200 \text{ GeV}$  40% to 80% centrality using equation 7. See text for complete information.

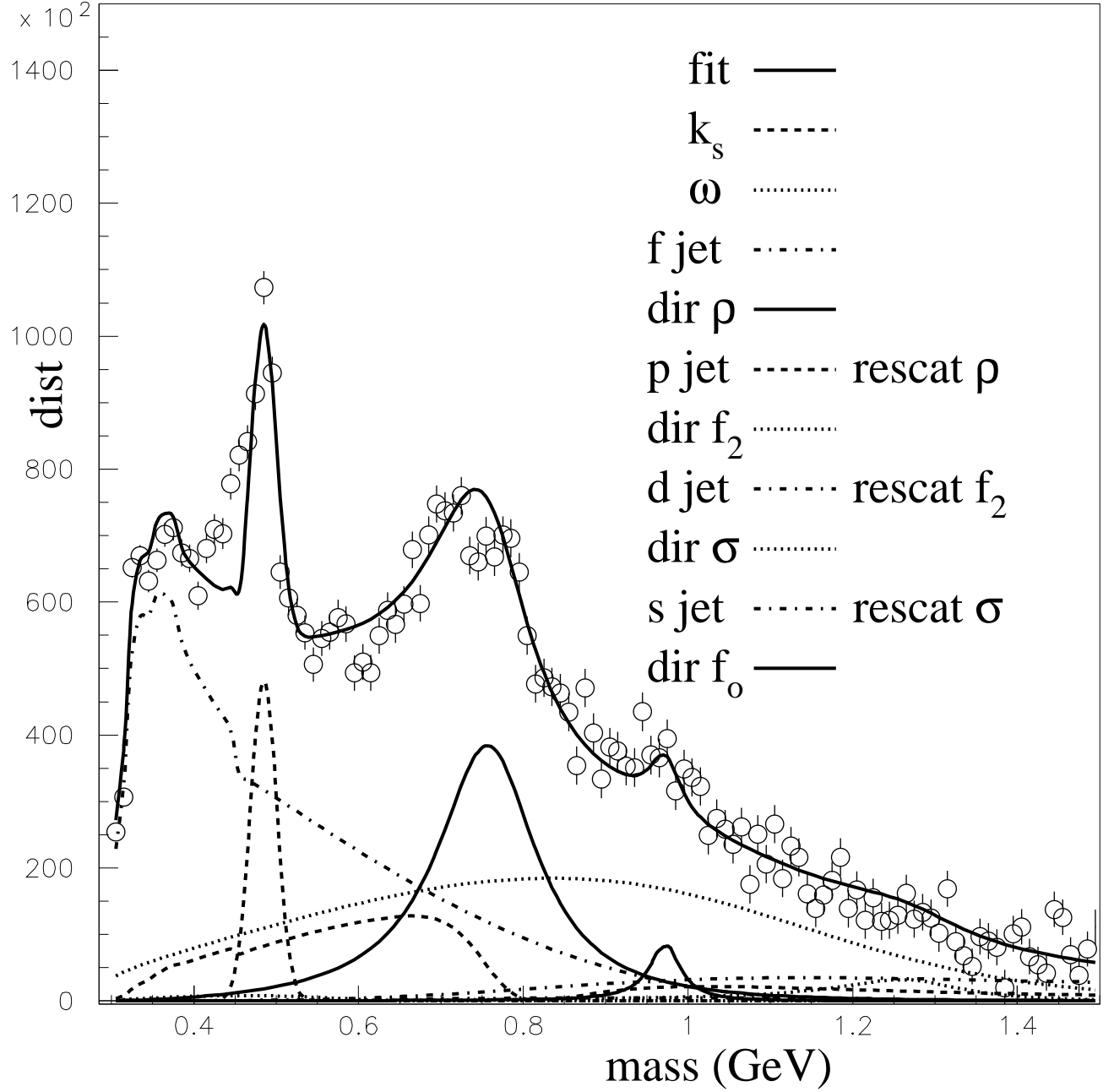


Figure 10: Fit to STAR dipion effective mass distribution ( $2.0 \text{ GeV}/c < p_t < 2.2 \text{ GeV}/c$ ) for Au-Au collisions at  $\sqrt{s_{NN}} = 200 \text{ GeV}$  40% to 80% centrality using equation 7. See text for complete information.



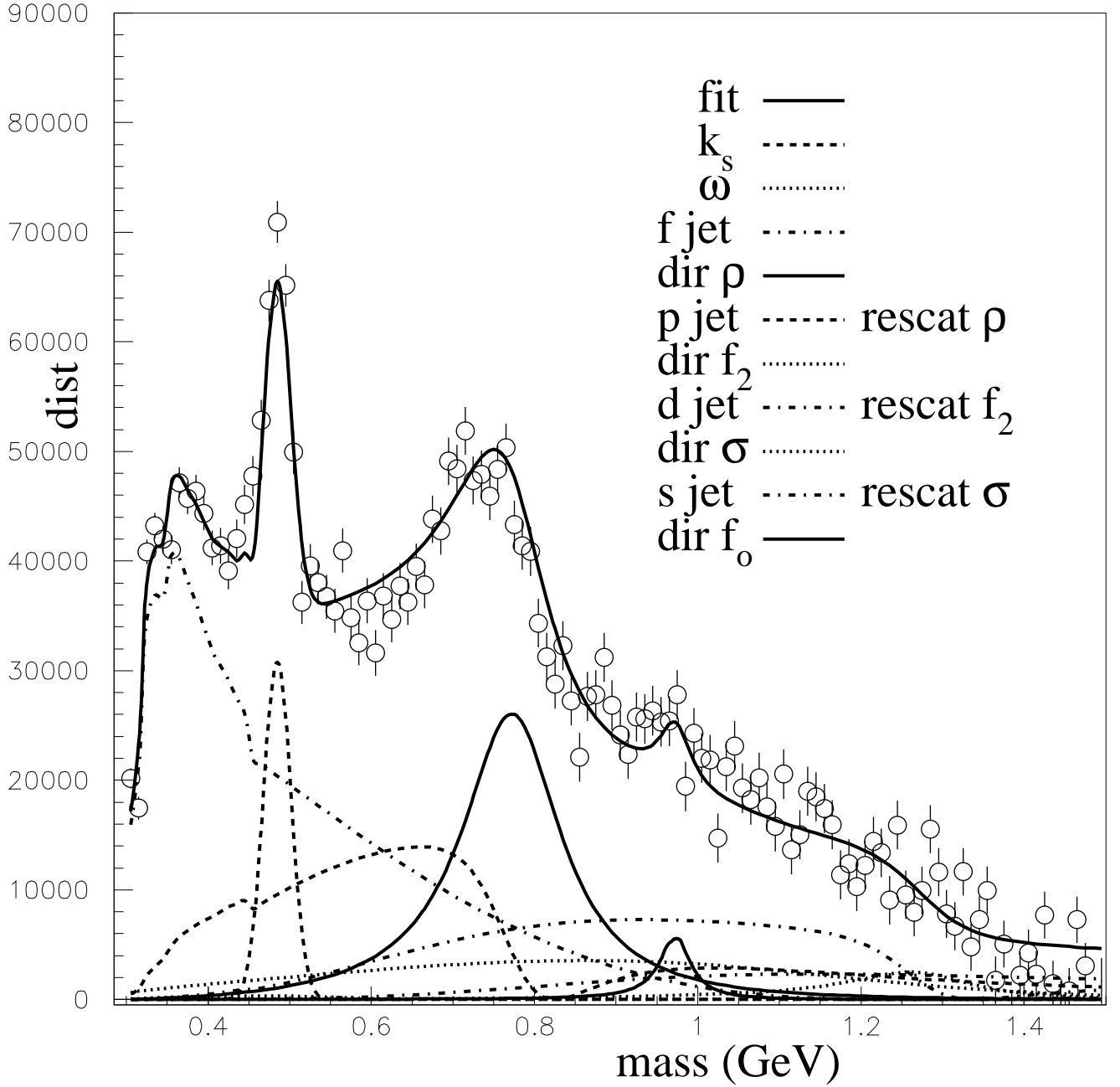


Figure 11: Fit to STAR dipion effective mass distribution ( $2.2 \text{ GeV}/c < p_t < 2.4 \text{ GeV}/c$ ) for Au-Au collisions at  $\sqrt{s_{NN}} = 200 \text{ GeV}$  40% to 80% centrality using equation 7. See text for complete information.

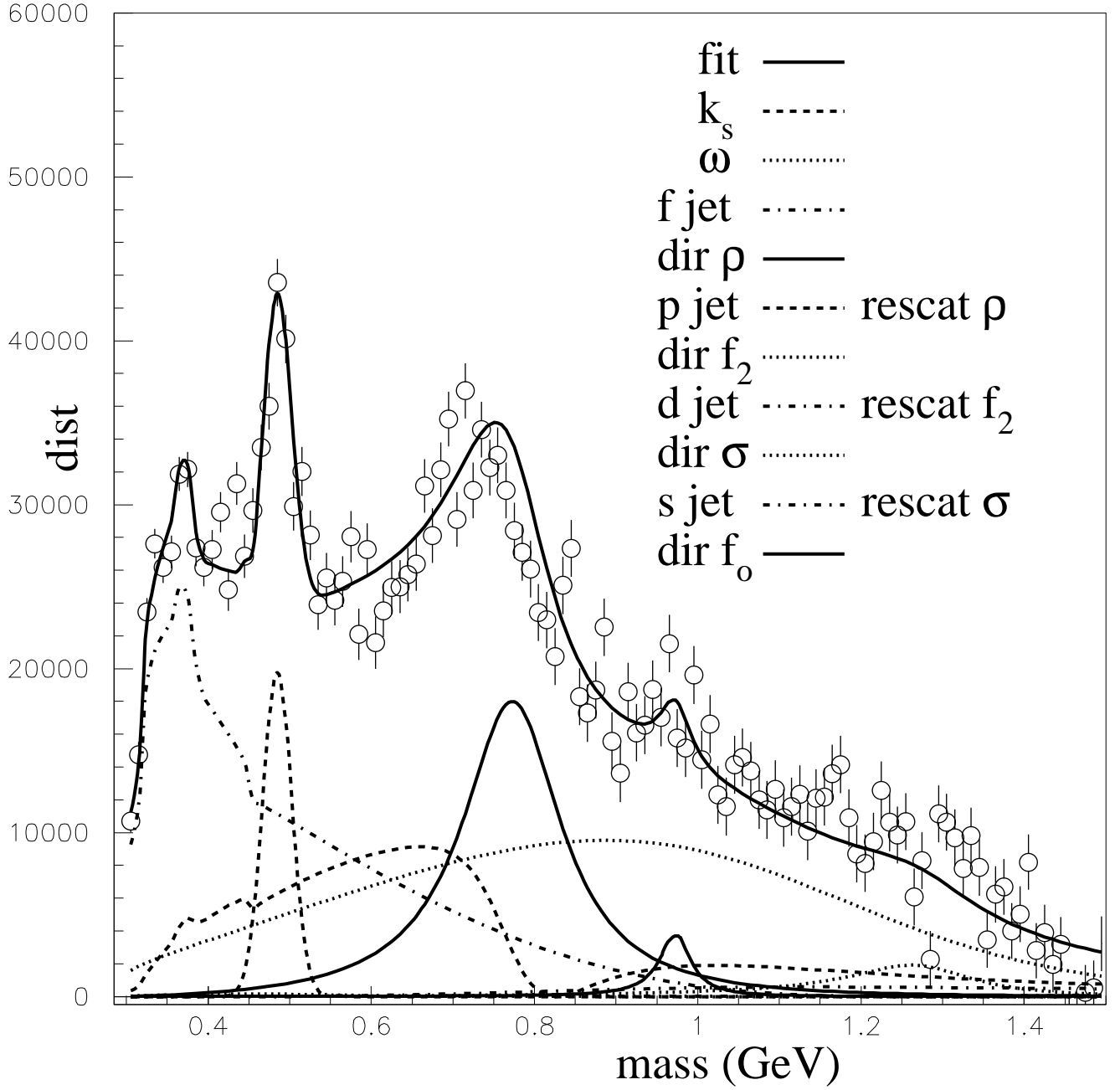


Figure 12: Fit to STAR dipion effective mass distribution ( $2.4 \text{ GeV}/c < p_t < 2.6 \text{ GeV}/c$ ) for Au-Au collisions at  $\sqrt{s_{NN}} = 200$  GeV 40% to 80% centrality using equation 7. See text for complete information.

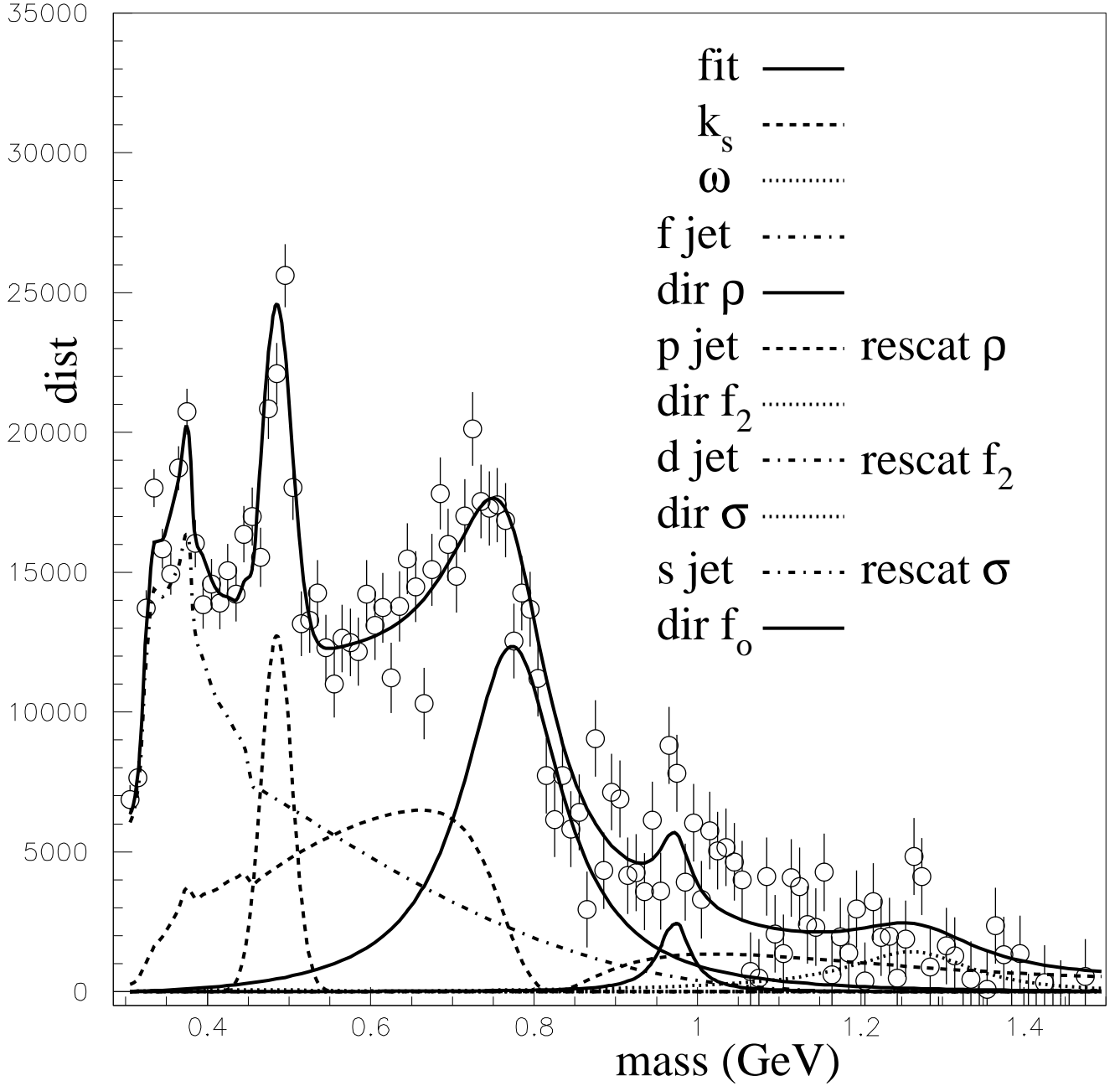


Figure 13: Fit to STAR dipion effective mass distribution ( $2.6 \text{ GeV}/c < p_t < 2.8 \text{ GeV}/c$ ) for Au-Au collisions at  $\sqrt{s_{NN}} = 200$  GeV 40% to 80% centrality using equation 7. See text for complete information.

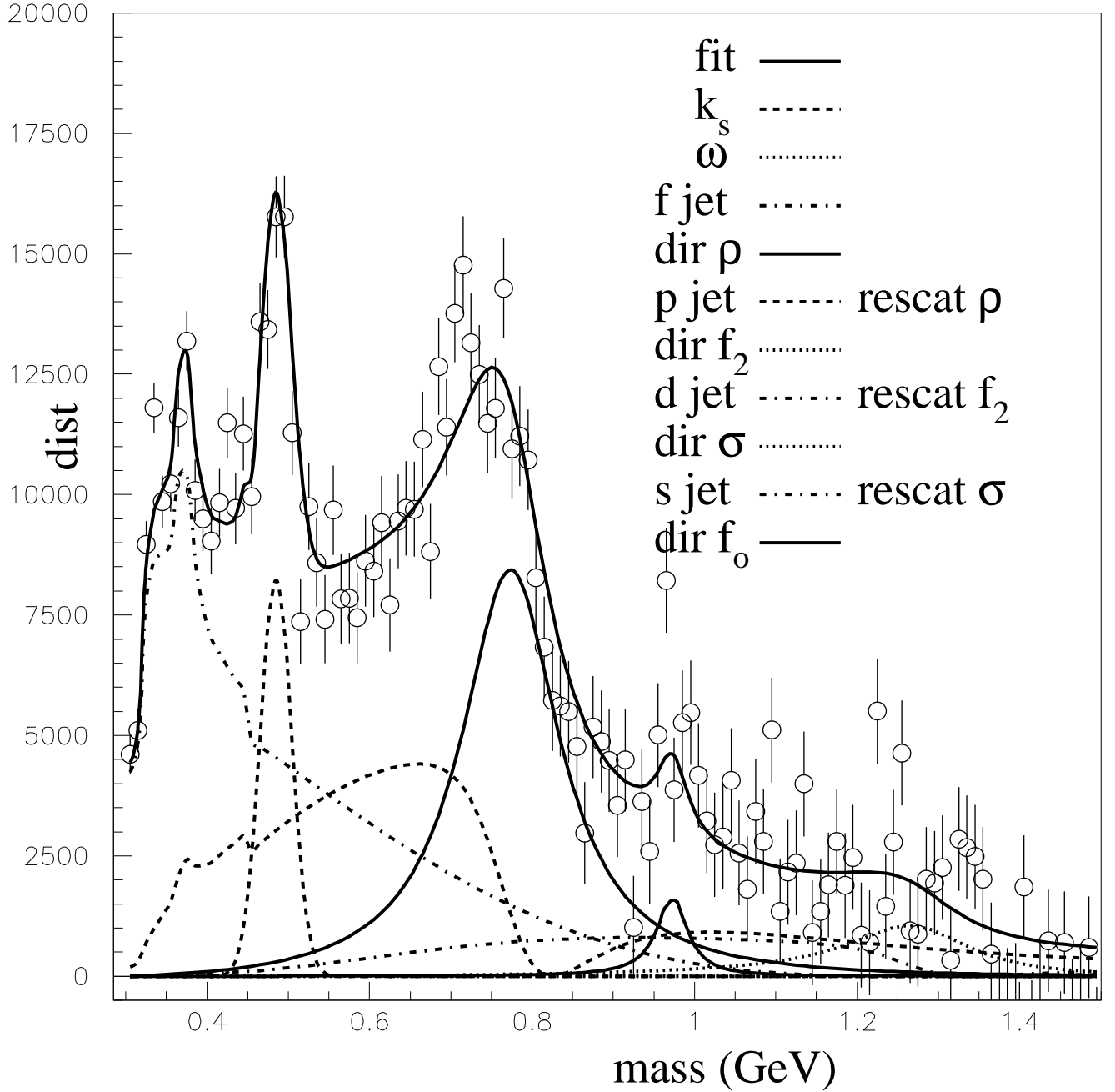


Figure 14: Fit to STAR dipion effective mass distribution ( $2.8 \text{ GeV}/c < p_t < 3.0 \text{ GeV}/c$ ) for Au-Au collisions at  $\sqrt{s_{NN}} = 200$  GeV 40% to 80% centrality using equation 7. See text for complete information.

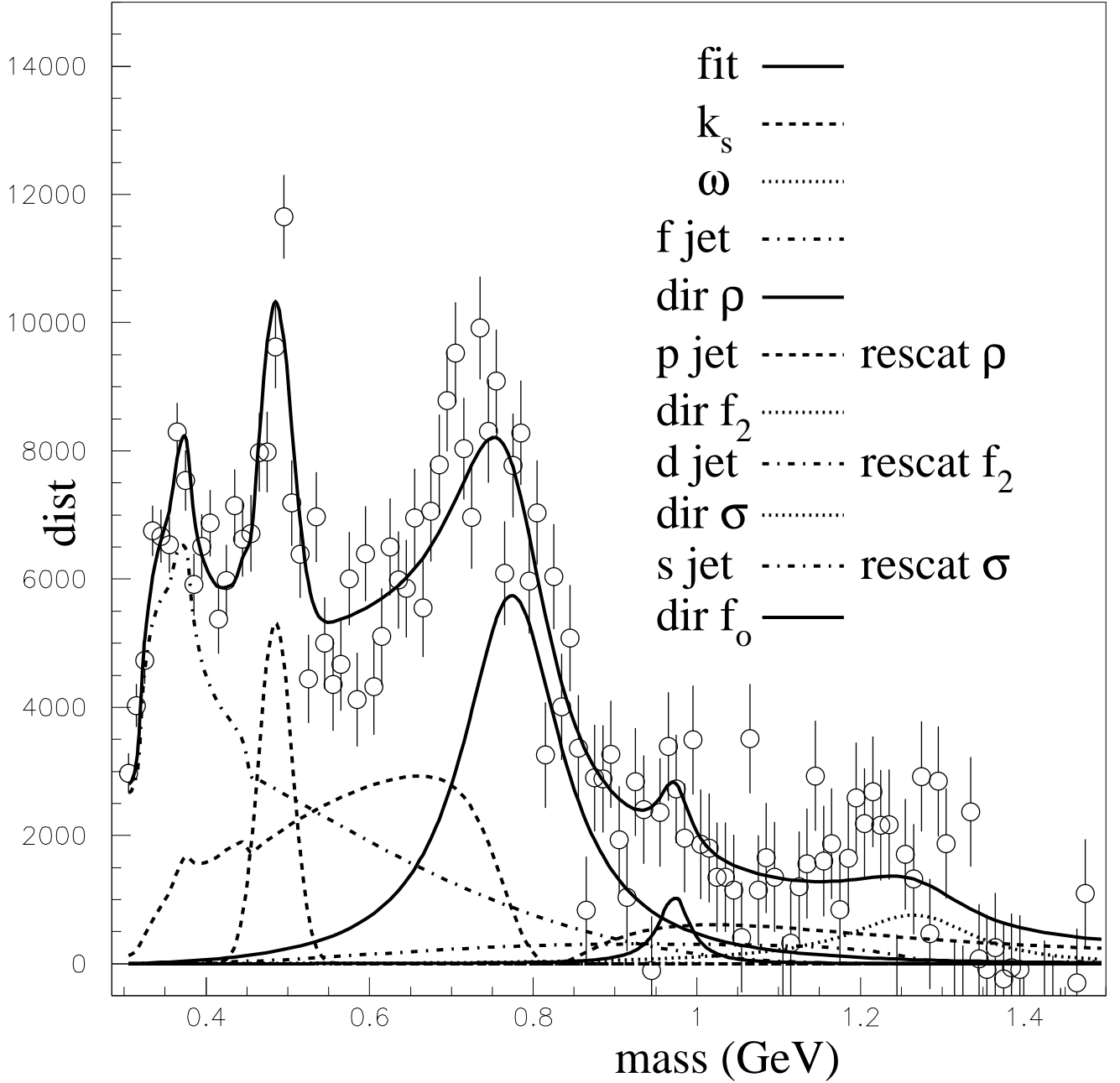
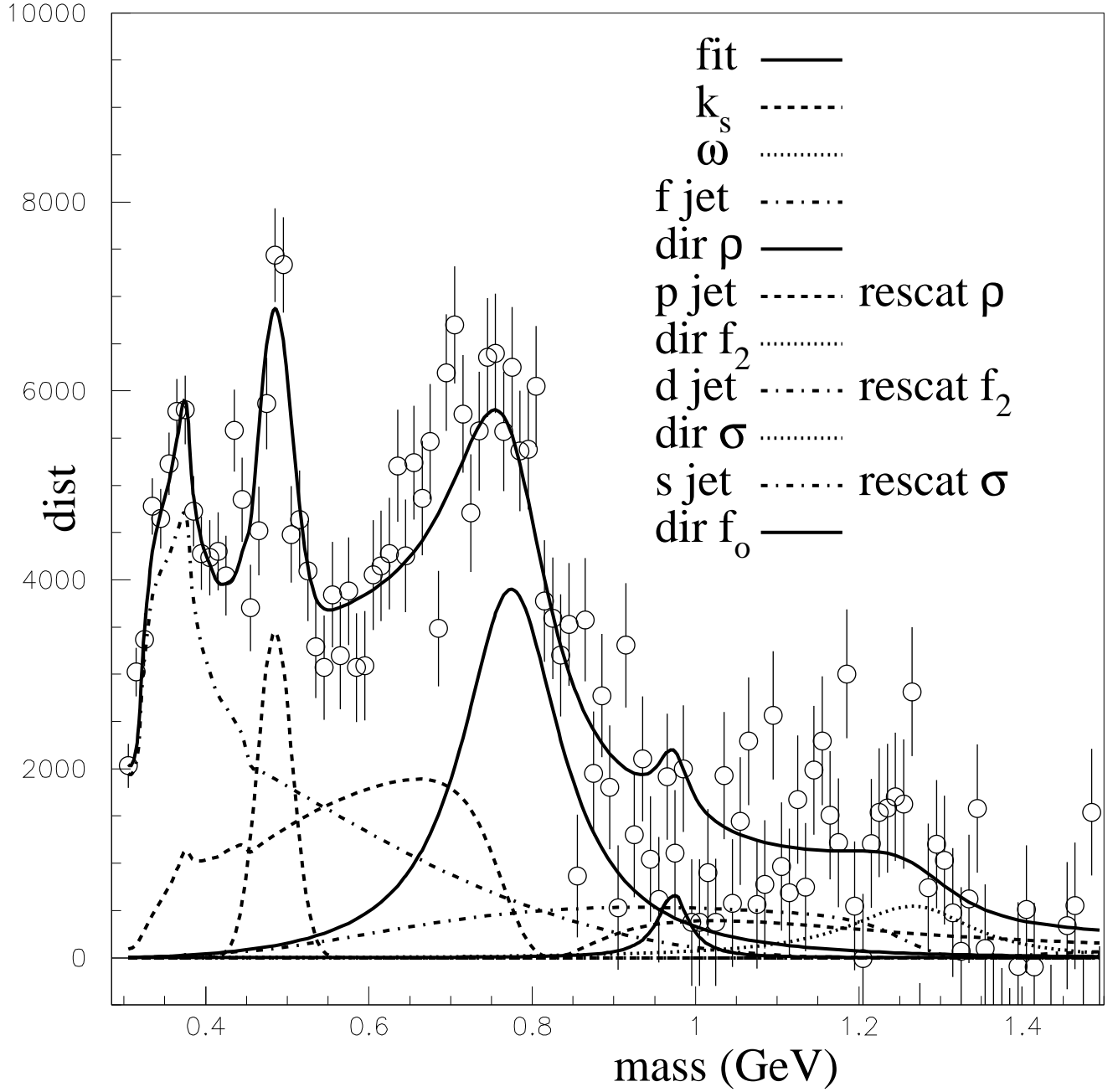


Figure 15: Fit to STAR dipion effective mass distribution ( $3.0 \text{ GeV}/c < p_t < 3.2 \text{ GeV}/c$ ) for Au-Au collisions at  $\sqrt{s_{NN}} = 200 \text{ GeV}$  40% to 80% centrality using equation 7. See text for complete information.



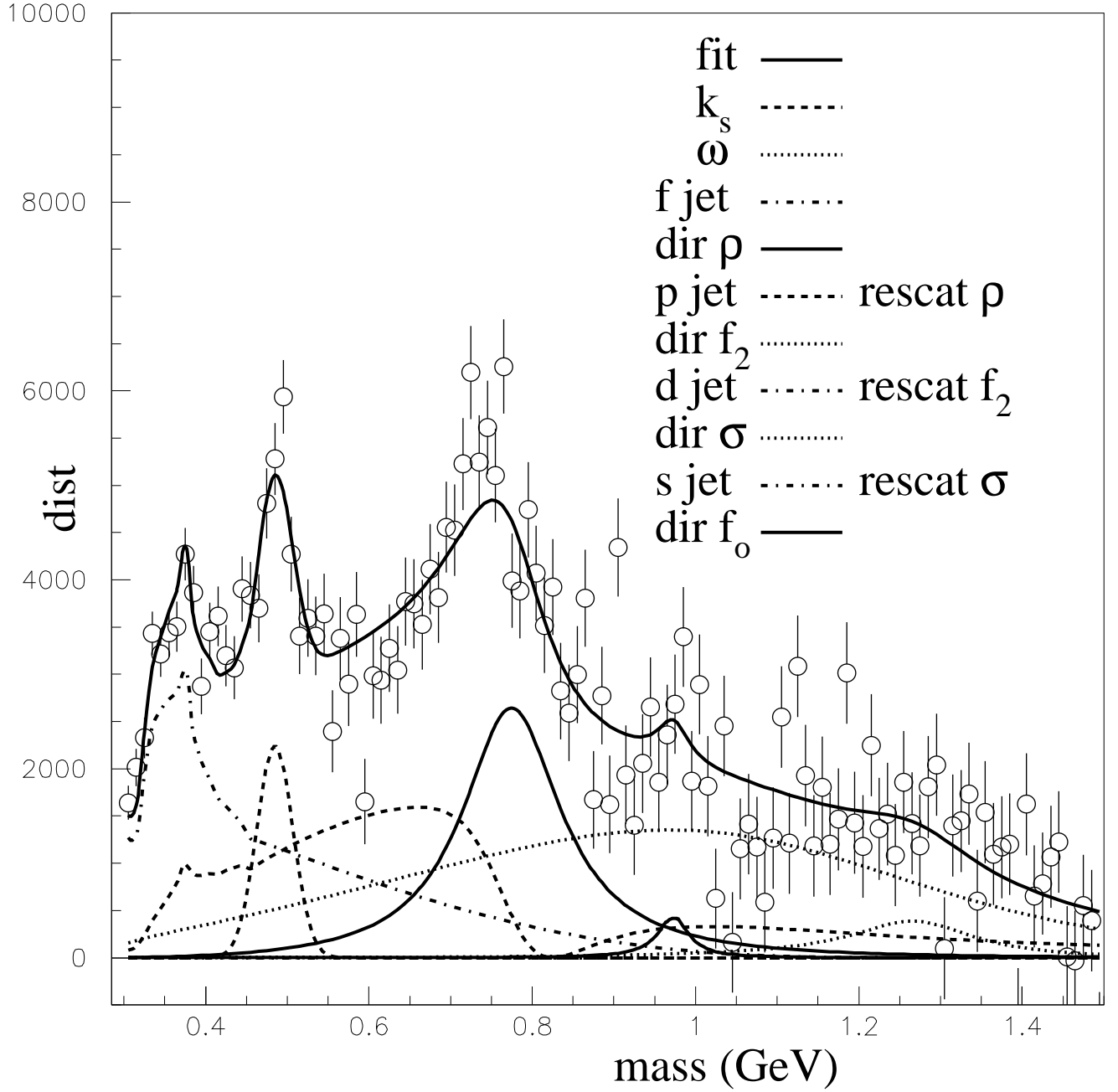


Figure 17: Fit to STAR dipion effective mass distribution ( $3.4 \text{ GeV}/c < p_t < 3.6 \text{ GeV}/c$ ) for Au-Au collisions at  $\sqrt{s_{NN}} = 200 \text{ GeV}$  40% to 80% centrality using equation 7. See text for complete information.

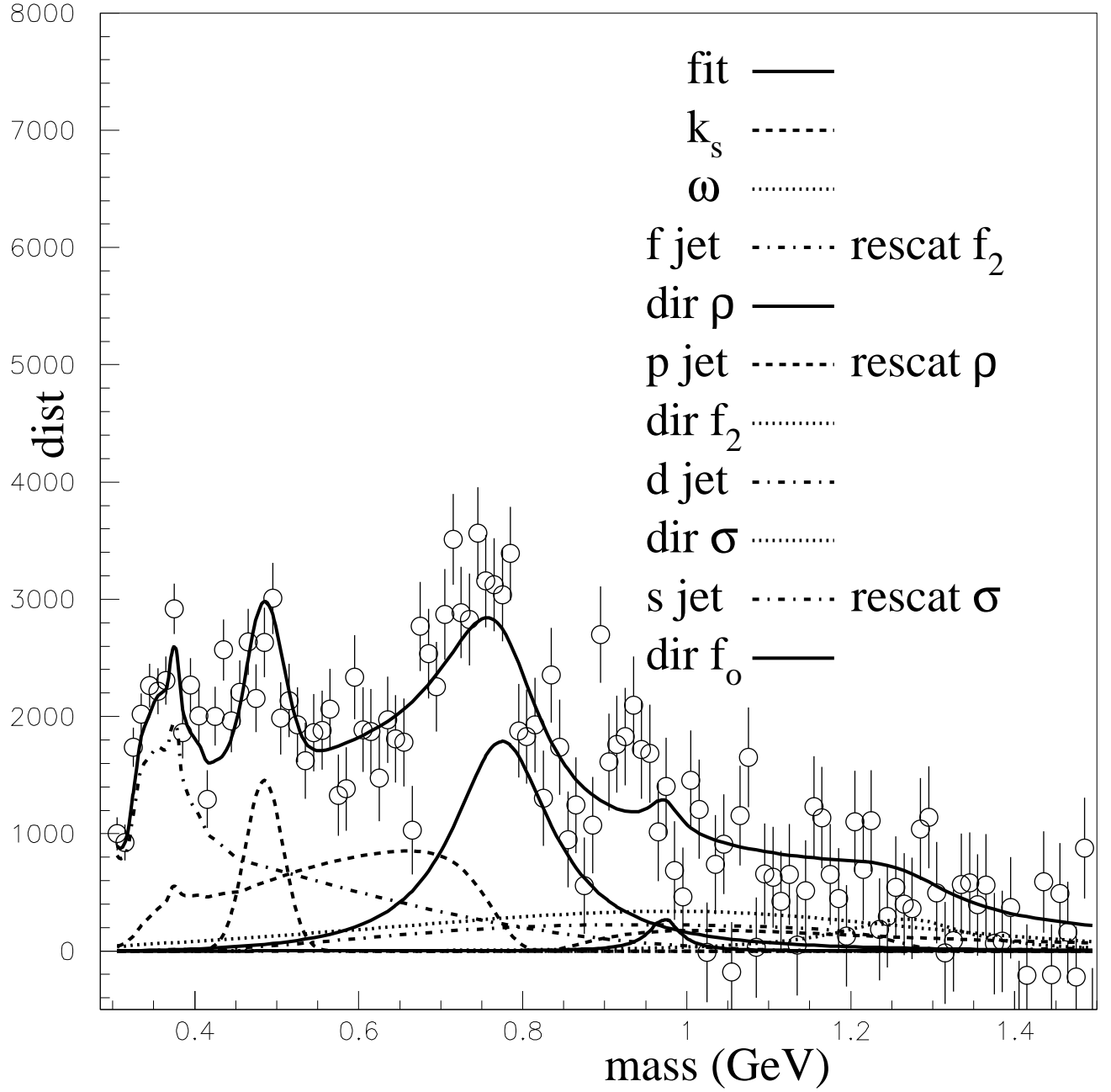


Figure 18: Fit to STAR dipion effective mass distribution ( $3.6 \text{ GeV}/c < p_t < 3.8 \text{ GeV}/c$ ) for Au-Au collisions at  $\sqrt{s_{NN}} = 200 \text{ GeV}$  40% to 80% centrality using equation 7. See text for complete information.



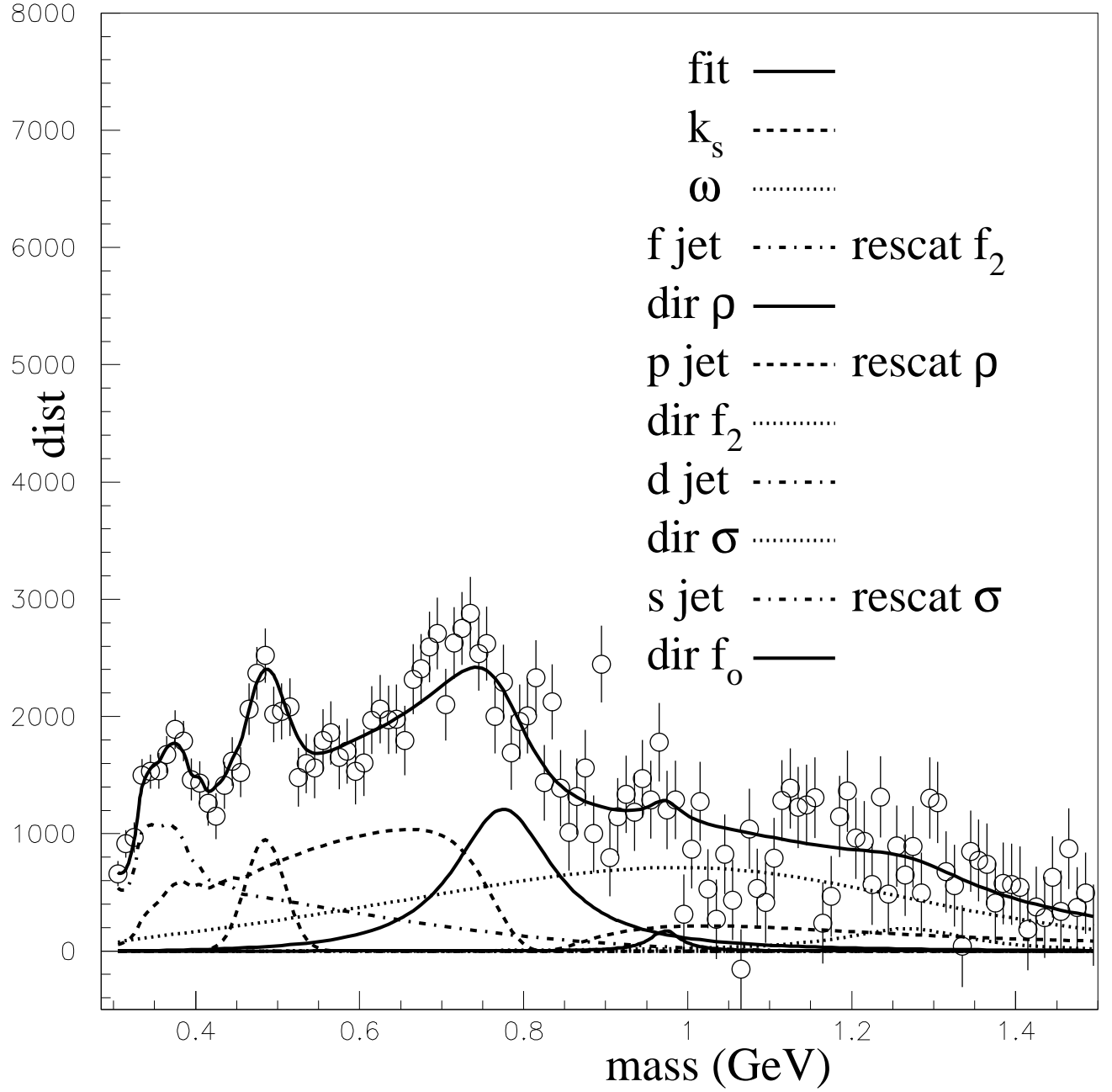


Figure 19: Fit to STAR dipion effective mass distribution ( $3.8 \text{ GeV}/c < p_t < 4.0 \text{ GeV}/c$ ) for Au-Au collisions at  $\sqrt{s_{NN}} = 200 \text{ GeV}$  40% to 80% centrality using equation 7. See text for complete information.

The direct cross sectional yield of the thermally produced states into  $\pi^+ \pi^-$  is shown in Figure 20. The states are  $k_s$ ,  $\rho$ ,  $f_0$  and  $f_2$  and the yields come from the exponential fits to the direct thermal component of equation 7.

## 5 Summary and Discussion

The Dipion Cocktail Part 2 applies a formalism derived in The Dipion Cocktail Part 1 which considered a mixture of sources present in the dipion mass spectrum of the heavy ion fireball. Part 1 showed that both thermal or soft production of hadrons and the minijet fragmented hadrons can be described through a set of unified formal equations. Part 2 (this paper) applies this Part 1 formalism to the  $p_t$  dependence of dipions for Au-Au collisions at  $\sqrt{s_{NN}} = 200$  GeV and 40% to 80% centrality.

Part 1 started with the basic definition of elastic  $\pi\pi$  scattering. Next showed how re-scattering of pions depends on the unitary condition that interactions present in the phase shift of an orbital state must interact all the time. The process of parton fragmentation into dipion states through unitarity leads to a equation of production and re-scattering in a given orbital quantum number. This equation (equation 7) has two components in each orbital state: one being the thermal production of resonances in a dipion orbital state, the other is the re-scattering of dipions coming from parton or minijet fragmentation into the dipion orbital state which do not come directly from the resonance. Unitarity requires that there must be re-scatter through resonance phase shifts which we defined through Breit-Wigner parameters (mass, width).

We have fitted 19 dipion  $p_t$  ranges (see Table I) using equation 7. We included minijets up to  $\ell = 3$  and resonances  $\sigma$   $\ell = 0$ ,  $\rho(770)$   $\ell = 1$ , and  $f_2(1270)$   $\ell = 2$ . Using the arguments of Sec. 3 of Part 1, we added the  $f_0$  as a direct thermal term ( $|T_0|^2_1$ ) and only the  $\sigma$  interfered with  $\ell = 0$  minijet background. Two other thermal terms are present in the cocktail, the  $k_s^0$  and the  $\omega_0$ . All the thermal terms have an exponential behavior with dipion  $p_t$  and are shown Figure 20. The spectrum of the minijet partial waves is obtained from PYTHIA[3] (see Sec. 5.2 of Part 1). We let the data determine which minijet partial wave to add. We find only Swave minijet background is important until  $p_t$  equal to 1.1 GeV/c. Above 1.5 GeV/c all four minijet partial waves are used up to Fwave. It should be noted Dwave and Fwave are small effects. We used PDG[4] for the  $f_2(1270)$  mass = 1.275 GeV and width = .185 GeV. The  $f_0$  was fitted obtaining mass =  $0.9727 \pm .0039$  GeV and width =  $0.04512 \pm 0.01128$  GeV. The  $\sigma$  mass and width used was fixed because it was ill determined. The mass used was mass = 1.011 GeV and width = 1.015 GeV.

For the  $\alpha$  parameter in  $p_t$  bins up to 1.1 GeV/c the minijet Swave interference is the determining factor. Above 1.1 GeV/c the Pwave interference becomes most important. The values of  $\alpha$  which gives a reasonable fit are shown in Table II.

We have determined that the  $\sigma$  pole or Breit-Wigner parameters is so far away from the real axis thus it is too short lived to be influenced by hadronic interactions. The  $\rho$  phase shift being of a life time comparable to hadronic interaction taking place becomes most sensitive.

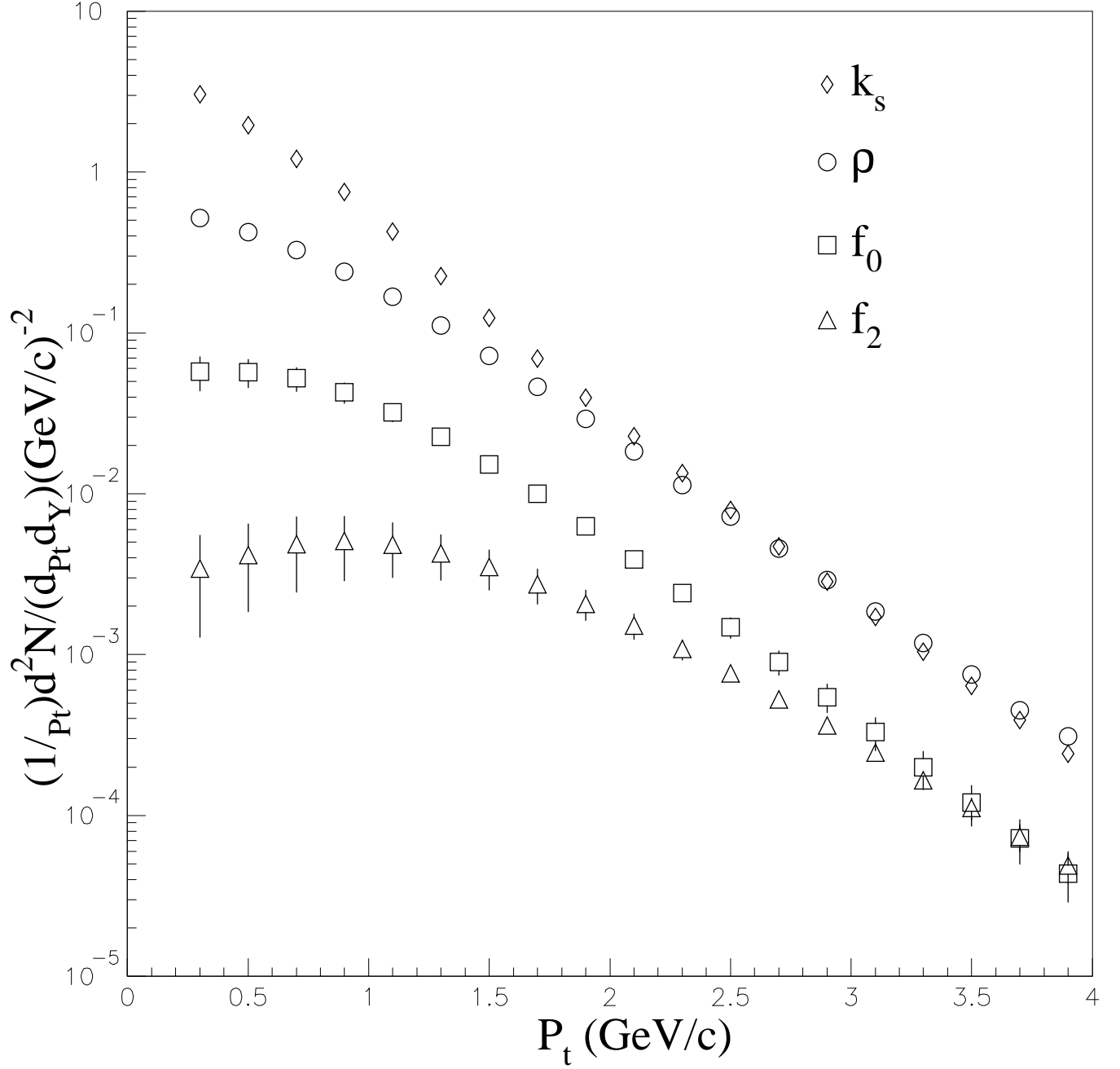


Figure 20: The direct thermal  $p_t$  yield into the  $\pi^+\pi^-$  channel as seen in the STAR dipion effective mass fit for the  $k_s$ ,  $\rho$ ,  $f_0$  and  $f_2$  using equation 7. See text for complete information.

We have found as a function of  $\alpha$  the best of  $\rho$  width is always 0.147 GeV with an error of  $\pm .007$  GeV. The mass however decreases as  $\alpha$  grows, reaching a minimum of 0.738 GeV at an  $\alpha$  of 0.907. This is a mass shift of 37 MeV. An  $\alpha$  of 0.504 is the smallest  $\alpha$  we find in our fits. A mass of 0.775 GeV is the best fit when the value of  $\alpha$  is at 0.504. Using equation 9 in Table II we determine the radius of  $\pi\pi$  re-scattering for each  $p_t$  range. Table II shows an interesting density effect around dipion  $p_t$  of 0.6 to 1.0 GeV/c. If one consider that  $p_t$  maybe related to fireball size through the idea of hubble flow, then pions with a  $p_t$  of around 0.4 GeV/c maybe coming from a less dense region in the central part of the fireball. This could be a density wave effect.

## 6 Acknowledgments

This research was supported by the U.S. Department of Energy under Contract No. DE-AC02-98CH10886. The author thanks William Love for the STAR analysis of the angular correlation data from Run 4. Also for his assistance in the production of figures. It is sad that he is gone.

## References

- [1] T. Trainor, Phys. Rev. C 80 (2009) 044901.
- [2] F. von Hippel and C. Quigg, Phys. Rev. 5 (1972) 624.
- [3] T. Sjostrand, M. van Zijil, Phys. Rev. D 36 (1987) 2019.
- [4] J. Beringer et al. (Particle Data Group), J. Phys. D86 (2012) 010001.